ADVANCED MATERIALS
www.advmat.de

Shift-Current Photovoltaics Based on a Non-Centrosymmetric Phase in In-Plane Ferroelectric SnS

*Yih-Ren Chang, Ryo Nanae, Satsuki Kitamura, Tomonori Nishimura, Haonan Wang, Yubei Xiang, Keisuke Shinokita, Kazunari Matsuda, Takashi Taniguchi, Kenji Watanabe, and Kosuke Nagashio**

The shift-current photovoltaics of group-IV monochalcogenides has been predicted to be comparable to those of state-of-the-art Si-based solar cells. However, its exploration has been prevented from the centrosymmetric layer stacking in the thermodynamically stable bulk crystal. Herein, the non-centrosymmetric layer stacking of tin sulfide (SnS) is stabilized in the bottom regions of SnS crystals grown on a van der Waals substrate by physical vapor deposition and the shift current of SnS, by combining the polarization angle dependence and circular photogalvanic effect, is demonstrated. Furthermore, 180° ferroelectric domains in SnS are verified through both piezoresponse force microscopy and shift-current mapping techniques. Based on these results, an atomic model of the ferroelectric domain boundary is proposed. The direct observation of shift current and ferroelectric domains reported herein paves a new path for future studies on shift-current photovoltaics.

1. Introduction

The lack of inversion symmetry in a crystal structure can give birth to a variety of unique characteristics. Following the discovery and exploration of non-centrosymmetric oxide materials, such as $BiTiO_3$ and $PbTiO_3$,[1,2] the non-centrosymmetric properties of low-dimensional materials have recently drawn intense attention. For example, second-harmonic generation (SHG),[3] piezoelectricity,[4,5] ferroelectricity,[6–8] and the bulk photovoltaic effect (BPVE),[9–11] are widely observed for many 1D or 2D materials and their heterostructures.[12] When these properties are combined with other advantages of low-dimensional materials, specific applications, such as high-power-density and flexible nanogenerators, sensors, and self-powered devices,[4,5,13] can be realized, which contributes to the pervasiveness of the Internet of Things (IoT). Among the non-centrosymmetric properties, the BPVE is especially focused on because of its wide range of applications, including not only power generators but also self-powered photodetectors.[14] Compared to common photodetectors based on low dimensional materials,[15,16] self-powered devices exhibit the advantage of power saving aspect since no external bias voltage is required for operation. Moreover, unlike the ordinary photovoltaic effect, wherein an internal electric field arises from heterostructures that consist of two or more material components,[17,18] the BPVE generates a photocurrent from a single component. This trait is beneficial for device fabrication since only one material has to be incorporated in the photoactive layer and no heterostructure formation is needed. Furthermore, the BPVE can produce high open-circuit photovoltages larger than the band gap energies of materials,[1,19] which indicates its potential for allowing the Shockley–Queisser limit to be overcome in single-junction solar cells.[20] The photocurrent from the BPVE, J_{BPVE}, generally consists of two parts, as shown in the following:[21]

$$J_{\mathrm{BPVE}} = \sigma_2 E^2 + \eta_2 E \times E^* \quad (1)$$

where σ_2 is the real component related to linearly polarized light, η_2 is the imaginary component related to circularly polarized light

Y.-R. Chang, R. Nanae, S. Kitamura, T. Nishimura, K. Nagashio
Department of Materials Engineering
The University of Tokyo
7-3-1 Hongo, Bunkyo, Tokyo 113–8656, Japan
E-mail: nagashio@material.t.u-tokyo.ac.jp
H. Wang, Y. Xiang, K. Shinokita, K. Matsuda
Institute of Advanced Energy
Kyoto University
Gokasho, Uji, Kyoto 611-0011, Japan
T. Taniguchi
International Center for Materials Nanoarchitectonics
National Institute of Materials Science
1-1 Namiki, Tsukuba, Ibaraki 305-0044, Japan
K. Watanabe
Research Center for Functional Materials
National Institute of Materials Science
1-1 Namiki, Tsukuba, Ibaraki 305-0044, Japan

The ORCID identification number(s) for the author(s) of this article can be found under https://doi.org/10.1002/adma.202301172

DOI: 10.1002/adma.202301172

and E is the electric field of light. The first term of Equation (1) is known as the shift current or linear photogalvanic effect, and its origin is considered to be the shift of photoexcited carriers in real space due to the difference in the Berry connection between the conduction and valence bands or the quantum coherent motion of a pair of dipoles moving in k space.[21,22] The second term of Equation (1) is the so-called ballistic current or circular photogalvanic effect (CPGE), which generates spin-dependent photocurrents depending on the helicity of light and disappears under linear polarization.[23,24] The origin of the CPGE current comes from the asymmetric velocity distribution in bands arising from the kinetic processes of asymmetric photoexcitation, recombination, and momentum relaxation.[21,25–27]

Recently, the shift current of low-dimensional materials has been extensively explored, and it was reported that spontaneous polarization as well as a non-centrosymmetric structure is necessary to observe the shift current.[9] This is because the spontaneous polarization and the shift current are closely related to each other through the Berry connection.[22,28] Although the understanding of the shift current has progressed, the value of the shift current that can be obtained from non-centrosymmetric material systems is generally small. Unlike conventional perovskite oxides that only show small shift currents ($BiFeO_3$: 0.05 μA V^{-2}, $BaTiO_3$: 5 μA V^{-2}), group IV monochalcogenides have recently been theoretically predicted to have much larger shift currents (≈100 μA V^{-2}), comparable to those of state-of-the-art Si-based solar cells (250 μA V^{-2}).[29–31] With a general formula of MX (where M = Ge, Sn and X = S, Se, Te), group IV monochalcogenides are 2D materials exhibiting anisotropic puckered structures, and when in monolayer form, they exhibit not only strong shift currents but purely in-plane piezoelectricity and ferroelectricity.[32,33] Among these materials, tin sulfide (SnS) was selected in this research because SnX is more chemically stable than GeX and the Curie temperature of monolayer SnS is higher than that of monolayer SnSe.[34,35] To date, although the piezoelectricity and ferroelectricity of SnS have been experimentally demonstrated,[4,6,36] the shift current of SnS has not yet been observed. The main reason for this could be the weakened in-plane spontaneous polarization with increasing material layer number due to the odd–even effect,[36–38] which has largely hindered the study and applications of the shift current of SnS.

In this work, the non-centrosymmetric structure of SnS was achieved in few-layer crystals on van der Waals substrates, and this achievement could be the key to solving the disappearance of the in-plane spontaneous polarization of bulk 2D materials. Known as the β' phase of SnS, this non-centrosymmetric structure was commonly observed at the interface between SnS grown by physical vapor deposition (PVD) and substrates, which indicates that the β' phase of SnS might be a stress-stabilized phase. With the assistance of angular-dependent measurement with polarized light, power-dependent measurement, and circularly polarized light with opposite helicity, the shift current of few-layer SnS was confirmed and distinguished from other kinds of spontaneous photocurrents. Moreover, an atomic model of the ferroelectric domain structure of SnS was proposed based on the observation of ferroelectric domains through both shift-current mapping and piezoresponse force microscopy (PFM) characterization. Our achievements based on the β' phase of SnS can provide deeper insight into the spontaneous polarization of ferroelectrics and facilitate the future progress of non-centrosymmetric property research in 2D materials.

2. Results and Discussion

2.1. Material Characterization

To obtain highly crystalline SnS, several improvements were made to the PVD growth conditions: i) van der Waals substrates, i.e., highly oriented pyrolytic graphite (HOPG), was used instead of mica substrates and ii) the growth rate was reduced by increasing the substrate temperature. The typical growth parameters are shown in Figure S1 (Supporting Information). The atomic force microscopy (AFM) image of a thin SnS crystal grown on HOPG under optimized parameters is shown in **Figure 1**a. Compared with typical SnS crystals grown on mica, as shown in Figure S2 (Supporting Information), the thin SnS crystal grown on HOPG exhibited a larger grain size with thermodynamically stable crystal facets, and these characteristics were observed even for a few-layer SnS with a thickness (t) of <10 nm. In this work, the largest grain size of PVD SnS with $t < 10$ nm was ≈5 μm.

In general, SnS crystals exhibit a centrosymmetric α phase (the antiferroelectric state of AB stacking layers, AB_{AFE}) because of its theoretically predicted lowest energy among the eight different phases.[39] As schematically illustrated in Figure S3 (Supporting Information), the eight different phases of SnS are generated by the combination of four different layer stacking orders (AA, AB, AC, AD) and two ferroelectric states (antiferroelectric (AFE) and ferroelectric (FE)). The adjacent SnS layers show the opposite polarization direction in the AFE state while exhibiting the same polarization direction in the FE state. In previous research, we experimentally demonstrated that ferroelectric SnS phases can be formed at the bottom region of bulk SnS crystals grown on mica substrates.[6] However, we were not able to determine their crystal structures because the AA_{FE} and AC_{FE} phases exhibit the same structure in the armchair direction, and the cross-sections of the SnS crystal structures were observed from only one direction by high-angle annular dark-field scanning transmission electron microscopy (HAADF-STEM). Given that the armchair and zigzag directions of SnS can be easily identified based on the clear facets shown in AFM images, the cross-sections of two individual SnS crystals grown on the same HOPG substrate were observed in two different directions, as shown in Figure S4 (Supporting Information). The cross-sectional HAADF-STEM images shown in Figure 1b clearly confirm that the non-centrosymmetric phase is not the AA_{FE} phase but instead the AC_{FE} phase. This non-centrosymmetric phase of SnS is also known as the β' phase, which was first observed in large bulk SnS crystals grown on a SiO_2/Si substrate by chemical vapor deposition.[40] Moreover, the layer number of the β' phase (AC_{FE}) on HOPG is 3–4 L, which is lower than that previously reported for the β' phase on mica (5–7 L).[6] This suggests that the stress-induced phase transition may be the origin of β' phase (AC_{FE}) formation. Actually, when the difference between the thermal expansion coefficients of SnS and substrates is taken into consideration ($13–16 \times 10^{-6}$ K^{-1} for SnS, 3×10^{-6} K^{-1} for mica, $4–8 \times 10^{-6}$ K^{-1} for graphite, and -0.81×10^{-6} K^{-1} for hexagonal boron nitride (h-BN)),[41–43] the tensile stress of the SnS layers near the SnS/HOPG interface is smaller

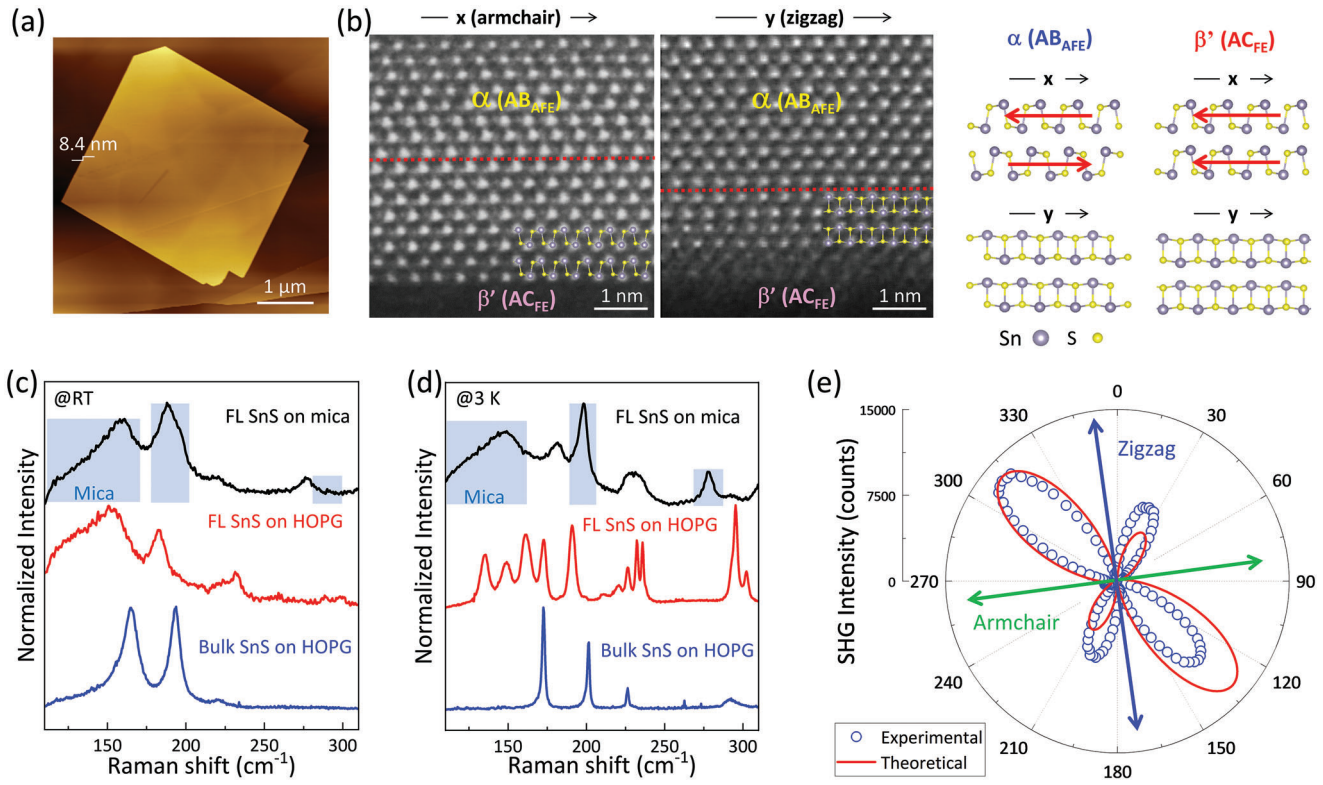

Figure 1. a) AFM topographic image of a typical SnS crystal grown on HOPG substrate. b) Cross-sectional HAADF-STEM images of few-layer SnS observed in the armchair direction and zigzag direction. The red lines mark the boundary of the α and β' phases. The schematic illustrations of crystal structures in the α and β' phases are compared on the right. c,d) Raman spectra of few-layer and bulk PVD SnS grown on mica and HOPG substrates measured at RT and 3 K, respectively. e) Parallel polarization SHG polar plot obtained from few-layer SnS. The red line is the theoretical calculation of the SHG intensity for bilayer β' phase. While the polarization angle dependence of SHG of bilayer and bulk β' phase were both calculated, the better agreement between experimental data and theoretical SHG intensity for bilayer β' phase suggests that the layer number of the β' phase in the sample is close to bilayer.

than that near the SnS/mica interface during the cooling process of material growth.[44] This result is in good agreement with our observation that a thicker β' phase (AC_{FE}) was formed on mica than on HOPG. The presence of the β' phase (AC_{FE}) near the substrate interface indicates that it might be stabilized by tensile stress since it is the second most stable phase among the eight phases of SnS.

The Raman spectra of few-layer SnS crystals with $t \approx 5$ nm grown on mica and HOPG are compared at room temperature (RT) and 3 K, as shown in Figure 1c,d. The Raman spectrum of the bulk PVD SnS crystal with $t \approx 30$ nm is also included as a reference for the α phase because the signal of the β' phase at the bottom region was blinded by the thick α phase on top. At RT, the Raman signals of the few-layer SnS crystal on mica were obscured by those of mica, while the Raman signals of the few-layer SnS crystal on HOPG were too broad to be distinguished. By reducing the measurement temperature to 3 K, sharp Raman peaks appeared for the few-layer SnS crystal on HOPG, while the few-layer SnS crystal on mica still showed broad Raman signals. This phenomenon indicates that PVD SnS can exhibit superior crystallinity when grown on a van der Waals substrate. Furthermore, the appearance of >10 Raman peaks at 3 K corresponds to recent first-principles calculation results, where 6 and 12 Raman vibration modes are predicted for the bulk α and β' phases, respectively.[45] Although the large number of peaks observed here is consistent with the prediction, the identification of Raman vibration modes was not achieved since the peak positions largely deviated from those obtained by theoretical calculations. This also suggests the existence of a large degree of stress in the SnS crystals. While the coexistence of α and β' phases in the same crystal was proven by cross-sectional HAADF-STEM images, the identification of Raman signals from both phases will be further analyzed in future work with the help of polarization-angle-dependent measurements and theoretically calculated Raman tensors. From the crystal thickness-dependent Raman spectra of SnS on HOPG shown in Figure S5 (Supporting Information), it was observed that the characteristic peaks of the β' phase disappeared gradually with increasing crystal thickness. The main cause of this phenomenon is the penetration depth of the 488 nm laser into SnS. Since the laser cannot reach the bottom layers of the SnS crystal, no Raman signals from the β' phase can be detected when the thickness of the SnS crystal is larger than the critical penetration depth of ≈15 nm. Therefore, it is appropriate to select the Raman spectrum of a 30 nm-thick SnS crystal as the reference for the α phase in this work, which is consistent with the Raman spectra for a bulk SnS flake exfoliated from a single-crystal grown by the horizontal gradient freeze method.[46]

To further support the existence of non-centrosymmetry in the β' phase, SHG spectroscopy was performed on the SnS crystals grown on HOPG. The SHG signal of SnS is expected to show angular dependency with linearly polarized light due to its anisotropic structure. In our experimental configuration, both the incident light and the collected SHG light were linearly polarized in the x–y plane (basal plane of SnS). As shown in Figure 1e, the parallel polarization SHG polar plot of the few-layer SnS fits well with the theoretical calculation results and is in good agreement with its crystal orientation (denoted in Figure S2e, Supporting Information). This result no doubt serves as clear evidence for the existence of a non-centrosymmetric structure in the β' phase. It should be noted that non-centrosymmetric properties, such as the SHG signal and ferroelectricity,[6] can still be observed for the few-layer SnS crystals with $t \approx 10$ nm even though the 3–4-layer-thick β' phase is covered by a much thicker α phase on top. This allows the following optical analysis and shifts current measurement of few-layer SnS crystals containing both α and β' phases.

2.2. Shift-Current Measurement

Since no bias between the source and drain electrodes is required for the shift-current measurement, the conductive HOPG substrate should be applicable for device fabrication. However, it turns out that neither small graphite flakes transferred onto the SiO_2/Si substrate nor the HOPG substrate could be utilized due to their large background current under zero bias conditions. Therefore, *h*-BN, an insulating van der Waals substrate, was applied instead as the growth substrate for SnS to avoid the generation of a large background current. Based on our previous SnS field-effect transistor (FET) device fabrication process,[47] SnS photocurrent devices were fabricated, as shown in **Figure 2**a. To avoid oxidation or degradation during the photocurrent measurement, *h*-BN flakes with thicknesses ranging from 10–20 nm were transferred on top to encapsulate the SnS devices, as schematically shown in Figure 2b.

To accurately measure the shift current of PVD SnS, the separation of the shift current from other spontaneous photocurrents is a critical issue. One of the primary sources of the spontaneous photovoltaic effect originates from the band bending caused by Schottky junction at the metal/2D contact region.[18,48] Since the Schottky junction photocurrent only appears at the contact region while the shift current can be observed throughout the whole non-centrosymmetric material,[9] one can easily separate them by avoiding photoillumination in the contact region. However, the separation of the photocurrent becomes difficult for short channel lengths smaller than 2 μm because photoillumination at the contact region is nearly inevitable for a fixed laser spot size (the ideal diameter of 0.66 μm in our experimental setup). As a result, the small lateral size of SnS grown on the *h*-BN substrate is a major issue. Although the enhanced growth conditions of SnS on HOPG mentioned previously were applied for the *h*-BN substrates, the lateral size was limited to several micrometers. This result corresponds to the observation that the typical lateral sizes of SnS crystals decrease in the order of HOPG, mica, *h*-BN, and SiO_2/Si substrates.[37,47,49] Therefore, as the first experimental improvement, linked SnS crystals aligned in the armchair direction of SnS were intentionally selected for device fabrication, as shown in Figure S6 (Supporting Information). It should be noted that the source and drain electrodes were also aligned in the armchair direction of SnS, which is the direction of spontaneous polarization. The second experimental improvement was the deposition of a 50 nm-thick Al film on top of the contact electrode region of the device, which was performed to prevent photoillumination in the Schottky junction region, as shown in Figure 2a,b. The high reflectivity of Al at 488 nm is effective for shading the incident laser in our experiment.[50] The spatially resolved photocurrent measurements were performed using an optical microscope with a prober system, as shown in Figure S7 (Supporting Information). Line scanning of the laser beam with a power of ≈100 μW was conducted using a digital micromirror device (DMD) with a 0.2 μm pitch. Figure 2c compares the line scan of photocurrents across the channel region of the SnS device with and without the Al cover film under a 0 V drain voltage (V_D) and 0 V back gate voltage (V_{BG}). The photocurrent under the Al film was obviously suppressed because of the weakened illumination, contributing to the better overall resolution of the shift-current measurement. Based on the optimized device structure, further analyses of the shift current of the SnS/*h*-BN devices were conducted.

Figure 2d shows the AFM image of the best SnS device with two-linked crystals, which was taken before the formation of the top *h*-BN layer and Al cover layer for easy viewing. The photocurrent line profile with a 0.2-μm pitch along the black dotted line in Figure 2d is shown in Figure 2e. Four distinct photocurrent peaks can be clearly distinguished from the line profile, and their origins are discussed in the following paragraphs. Although the Al cover reduced the illumination at the contact region of SnS, a small Schottky junction current was still observed and led to the photocurrent peaks observed at the edge of the Al film. To further separate these photocurrents, the angular-dependent measurement of linearly polarized light was introduced. Since the absorbance of SnS for linearly polarized light at 488 nm is nearly isotropic in all crystal directions,[51] the Schottky junction current is expected to be isotropic at all angles. On the other hand, because the shift current originates from the non-centrosymmetric structure of materials, an anisotropic shift current varied with polarization angles of linearly polarized light is expected, as reported in previous works.[9,10] According to the BPVE theory[52] and third-order tensor model developed by Fridkin et al,[2] the shift current in the i direction can be expressed as:

$$J_i = \beta_{ijk} E_j E_k = I \beta_{ijk} e_j e_k \tag{2}$$

where β_{ijk} is the shift current tensor, e_j and e_k are the projections of the electric field in the j and k directions, respectively, and I is the light intensity. Therefore, the shift current generated in the armchair direction of the SnS crystal when incident light is perpendicular to its basal plane can be further expressed by the following equation:[53,54]

$$J_3 = I \cdot \beta_{31} \sin^2\theta + I \cdot \beta_{33} \cos^2\theta \tag{3}$$

where β_{31} and β_{33} are the shift-current tensor elements of SnS and θ is the angle between the polarization direction of incident light and the armchair direction of SnS. The detailed derivation of Equation (3) is included in Note S1 (Supporting Information).

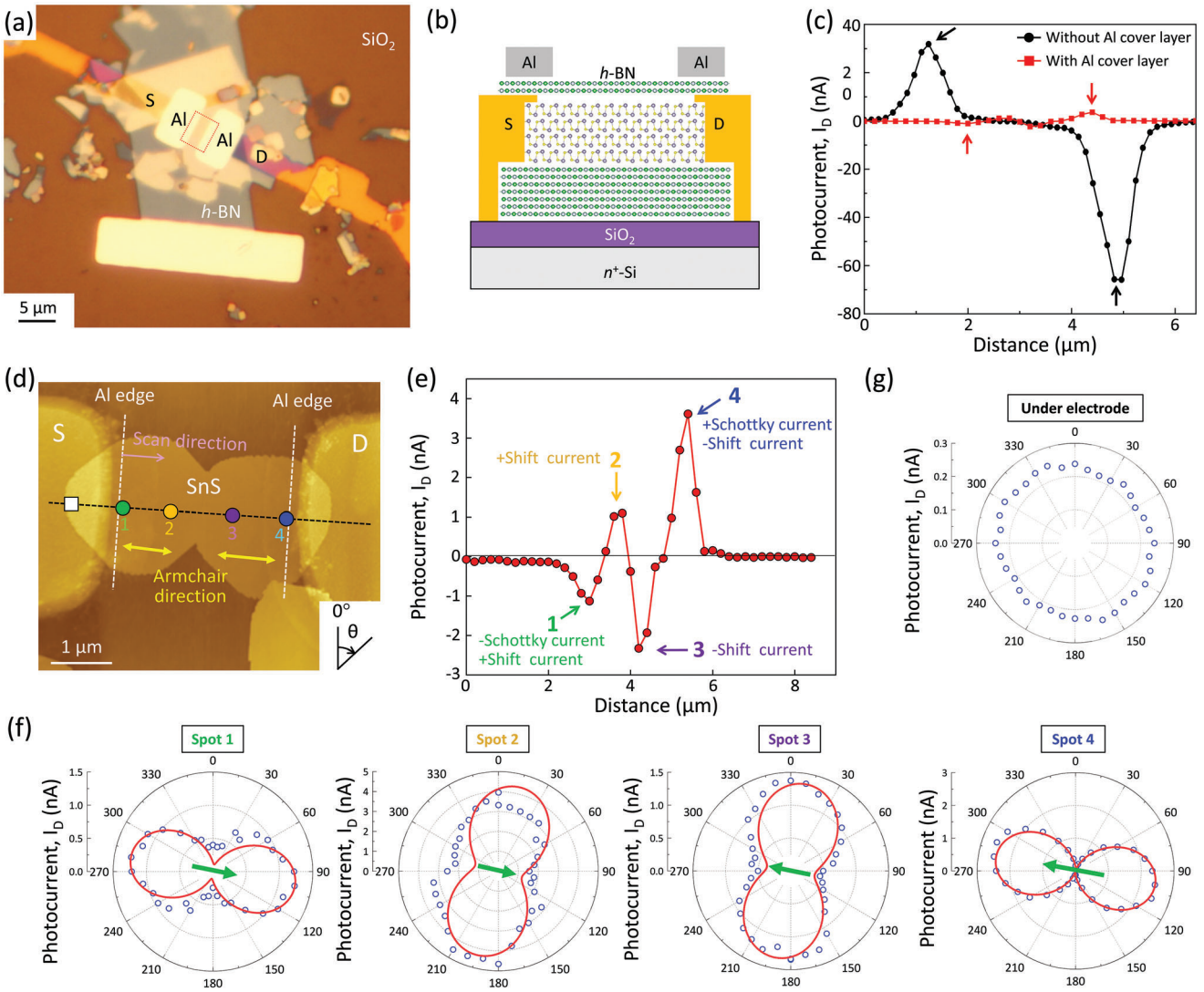

Figure 2. a) Optical microscopy image of a typical SnS shift-current device. b) Schematic illustration of the cross-sectional view of the SnS device. c) Photocurrents obtained from line scans across the channel region of the SnS device with and without an Al film on top. d) AFM topographic image of an SnS device with two-linked crystals measured before the application of *h*-BN encapsulation and Al film. e) Photocurrent obtained from the drain electrode under $V_D = 0$ V and $V_{BG} = 0$ V along the black dotted line shown in (d). The corresponding positions of the current peaks are marked in (d) with the same color, and the photocurrent origins of these current peaks are noted. f) Angular-dependent photocurrents induced by linearly polarized light measured at spots 1–4. The red lines are the calculated results of the shift current at spots 2 and 3 and the combination of the Schottky junction photocurrent and shift current at spots 1 and 4. The predicted spontaneous polarization direction is marked by green arrows. g) Angular-dependent photocurrent induced by linearly polarized light measured at the electrode region covered by Al film, whose position is indicated by the white rectangle in (d).

Based on the DFT calculation,[29] the shift-current tensors β_{31} and β_{33} of SnS under 488 nm irradiation are extracted as 60.8 μAV^{-2} and 16.9 μAV^{-2}, respectively. Therefore, the angular dependence of the theoretical shift-current intensity of SnS can be obtained. As shown in Figure S8 (Supporting Information), the intensity of the shift current generated in the armchair direction of the SnS crystal is anticipated to be the strongest when the polarization direction of incident light is parallel to the zigzag direction of SnS.

The polarization angle dependence of the shift current was analyzed at the four different spots showing photocurrent peaks in Figure 2e, and the results are shown in Figure 2f. A half-wave plate was utilized to switch the polarization direction in this experiment, as shown in Figure S7 (Supporting Information). It should be noted that the position of $\theta = 0$ was defined in Figure 2d, and the photocurrent in Figure 2e was measured at the drain electrode under the condition that the polarized direction of incident light was parallel to the zigzag direction of SnS. The photocurrents measured at spots 2 and 3, which were located in the channel region, showed strong angular dependence. Furthermore, it was observed that the polarized directions of higher current at these spots were parallel to the zigzag direction of the SnS crystals, which is in good agreement with the theoretical calculation. These results indicate that the photocurrent obtained here

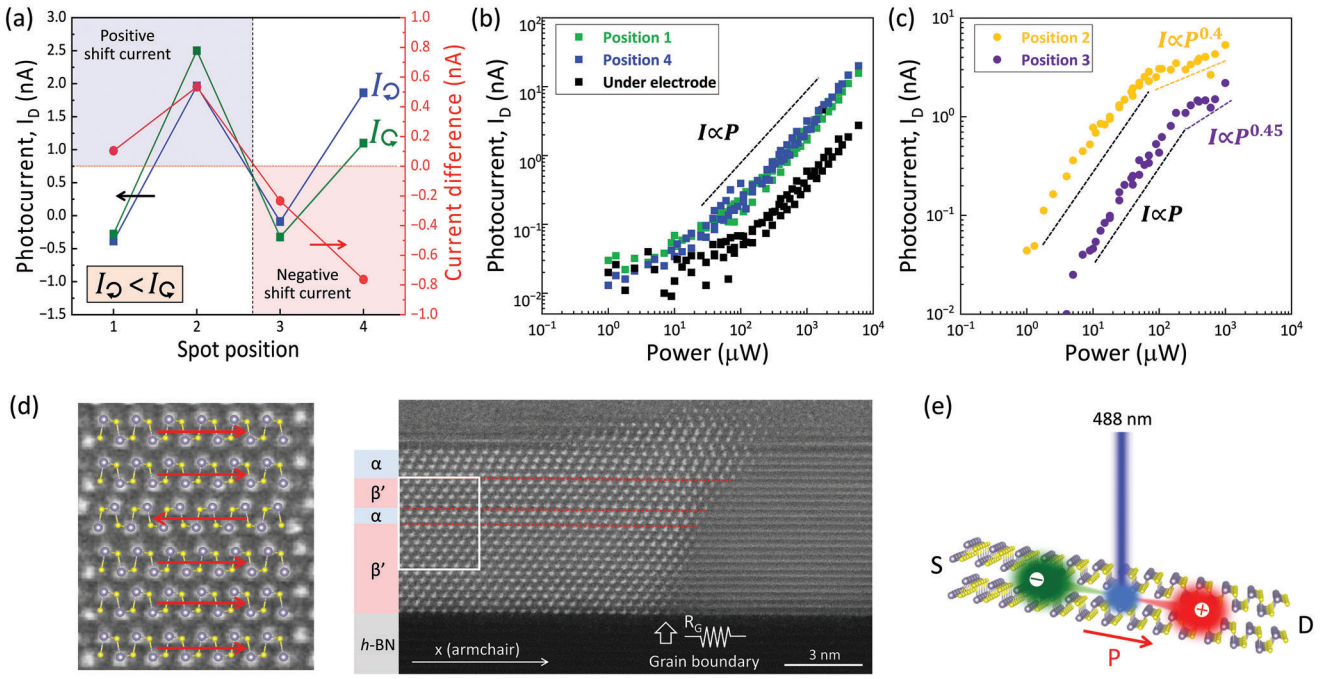

Figure 3. a) CPGE current obtained from circularly polarized light with opposite helicity at the same spots shown in Figure 2d. The red circles represent the difference between the CPGE currents induced by counterclockwise and clockwise circularly polarized light illumination. b,c) Power-dependent photocurrents at the spots shown in Figure 2d. d) Cross-sectional HAADF-STEM images in the armchair direction of the same SnS device shown in Figure 2d. The transition area between the β' and α phases is magnified with the corresponding crystal structure and spontaneous polarization direction denoted. The structure of the right crystal cannot be clearly observed due to the slight deviation in crystal orientation, and the grain boundary can be regarded as a resistance during the photocurrent measurement. e) Schematic illustration of shift-current generation under illumination with a 488 nm laser and the corresponding direction of current flow.

is mainly composed of the shift current of SnS crystals. On the other hand, at spots 1 and 4, the polarization angle dependency of the photocurrents did not match that at spots 2 and 3. The directions of higher photocurrents were perpendicular to those at spots 2 and 3. To verify this, another spot under the source electrode was measured as a reference for the Schottky junction photocurrent, whose position is shown by the open black rectangle in Figure 2d. Since no angular dependence in the Schottky junction photocurrent is expected,[51] it is reasonable to observe the isotropic photocurrent at source electrode area, as shown in Figure 2g. This result suggests that the photocurrents at spots 1 and 4 do not come from the Schottky junction alone. One plausible origin of the abnormal polarization angle dependency in photocurrents measured at spots 1 and 4 could be the combination of both the Schottky junction current and the shift current. Taking the photocurrent in spot 4 as an example, if a positive Schottky junction current with a slightly higher value and a negative shift current can be superimposed, the resulting photocurrent indeed shows a pattern similar to those experimentally obtained, as shown in Figure S9 (Supporting Information). Similarly, the photocurrent measured at spot 1 could come from the superimposition of the negative Schottky junction photocurrent and positive shift current. Through deconvolution, the directions showing higher shift currents at spots 1 and 4 are actually well-matched with the crystal orientations of the SnS crystals.

To further support the existence of the shift current, two additional characterization experiments were conducted. The first pertained to the utilization of the CPGE current represented by the second term in Equation (1). For the CPGE, it has been reported that the photocurrent intensity depends largely on the helicity of light.[23,24,55,56] While spin-up carriers are stimulated by light of a certain helicity, light of the opposite helicity induces spin-down carriers. Briefly, the CPGE describes the generation of spin-dependent photocurrents whose flow direction switches with the helicity of incident light. Taking advantage of the fact that the relationship between the CPGE current and shift currently in Equation (1) is retained in the same crystal,[27] the CPGE current can be applied to confirm the sign of the shift current predicted based on the polarization angle-dependent photocurrent measurement shown in Figure 2f. The experimental setup for the CPGE is the same as that for the abovementioned shift-current measurement except for the application of a quarter-wave plate, as shown in Figure S7 (Supporting Information). **Figure 3**a shows the photocurrents obtained from the four spots shown in Figure 2d under the illumination of circularly polarized light with opposite helicity. Clockwise and counterclockwise circularly polarized light indeed led to different photocurrent intensities at the same spots. First, spots 1 and 2 in the same crystal were focused on. At spot 2, the sign of the shift current was determined to be positive because the shift current was the only source of the positive photocurrents induced by linearly polarized light. To match the sign of the CPGE with that of the shift current, the sign of the CPGE under this measurement condition was defined as the photocurrent difference between the counterclockwise CPGE and clockwise CPGE, which was positive, as shown by the red dot at spot 2 in Figure 3a. Following the same definition, the sign of

the CPGE at spot 1 where the shift current was embedded by the Schottky junction current was considered. The positive sign of CPGE at spot 1 indicates that the sign of the shift current here is also positive. Although the positive sign of the shift current at spot 1 was determined by conjecture from the polarization angle dependence measurement, this assumption was supported by the present CPGE experiment. For spots 3 and 4, the situation is the opposite. The negative sign of CPGE here indicates the negative shift current at these spots. Moreover, it should be noted that the existence of the CPGE photocurrent indicates Rashba splitting in the electronic bands of β' SnS.[25,57]

The second method for characterizing the shift current was to investigate the incident light power dependency of the photocurrent.[9,10,58] The relationship between the total photocurrent J_{ph} and the incident light power P_{laser} can be simplified as follows:

$$J_{ph} = L \cdot P_{laser} + S_0 \cdot \frac{P_{laser}}{\sqrt{S_1 \cdot P_{laser} + S_2}} + J_0 \quad (4)$$

where L is the amplitude of the Schottky junction photocurrent, which shows a linear contribution; S_0, S_1, and S_2 characterize the shift-current contribution; and J_0 is the experimental offset of the measurement system.[22,58] The power-dependent photocurrents measured at the Al-covered contact region under the electrode and at spots 1 and 4 in Figure 2d are shown in Figure 3b. Since the photocurrents measured at these spots arose solely or mainly from the Schottky junction, their photocurrents showed a linear relationship with increasing light power. On the other hand, as shown in Figure 3c, the photocurrents measured at spots 2 and 3 showed a gradually decreasing slope in the high-power region, indicating that the photocurrents originated from the shift current of SnS. The relationships between the photocurrent and laser power at spots 2 and 3 were estimated to be $J \propto P^{0.4}$ and $J \propto P^{0.45}$, respectively. The slight deviation from the ideal dependence of $J \propto P^{0.5}$ might have resulted from other factors, such as the photothermal effect induced by local heating from the laser.

In the above shift-current experiment, two-linked SnS crystals, which were large enough for the measurement, were analyzed because of the lack of single-grain SnS crystals. The grain boundary of the two-linked SnS crystals was analyzed by HAADF-STEM, as shown in Figure 3d. With the crystal orientation determined based on the macroscopic crystal shape observed by AFM, the armchair structure was realized for the left SnS crystal. Although the crystal structure was not clearly observed for the right SnS crystal due to the slight deviation in crystal orientation, the SnS layers of the right crystal connected well with those of the left crystal at the grain boundary. Based on this observation, it is reasonable to consider that the grain boundary works just as the small resistance (R_G) during the shift-current measurement. Besides, it is quite interesting that multiple transitions between the β' and α phases were observed. Since only a single transition from the β' to α phases have been observed for all our isolated SnS crystals thus far, this transition may be triggered by the interaction of the SnS crystal with the neighboring crystal during PVD growth. In addition, the relationship between the direction of spontaneous polarization in the crystal and the direction of the shift current was elucidated. While this relationship depends on the Berry phase of the bands involved in the optical transition, it is known that the shift current is reversed depending on the excitation wavelength and the polarization direction in some materials.[59] The spontaneous polarization direction of the left SnS crystal was verified and is schematically illustrated in Figure 3e. The spontaneous polarization and shift-current directions are the same in SnS crystals under our experimental conditions.

2.3. Ferroelectric Domain

Since the formation of ferroelectric domains reduces the energy raised by spontaneous polarization by minimizing electrostatic and elastic energies,[60,61] the domain structure of SnS is discussed here. As shown in **Figure 4**a, the PFM image reveals that the widths of the ferroelectric domains in the few-layer SnS crystal range from 100 nm to 500 nm, which corresponds to the results of previous research.[62] Furthermore, it can be found that the ferroelectric domain boundaries are parallel to the crystal facet plane of SnS, which is energetically favorable. While the odd–even effect on spontaneous polarization in few-layer SnS,[36,62] and ferroelectric domain switching in monolayer SnSe[63] have been reported, there is no discussion of the ferroelectric domain structures on the atomic scale to date. Although the ferroelectric domain boundary structure has been reported for classical ferroelectric perovskite oxides in detail, the case of SnS is quite different. Taking $BaTiO_3$ as an example,[64] the spontaneous polarization depends on the position of the metal cation at the center of the unit cell, which restricts the polarization direction to one dimension and limits the polarization switching to 180° only. On the other hand, the spontaneous polarization in SnS results from the distortion of the puckered structure, which originates from the cubic NaCl structure through the breaking of the ionic bonds indicated by the dotted lines in Figure 4b.[65] Since the polarization switching of SnS takes place through the recovery of the cubic NaCl structure and "rediscconnection" of the bonds, the 90° switching of the in-plane spontaneous polarization is also possible, which leads to the ferroelectricity and ferroelasticity of SnS.[32,33] Based on the PFM results, the ferroelectric domain structures of SnS are explored through atomic models with two constraint conditions, as shown in Figure S10 (Supporting Information). First, twin boundaries[66] are considered to reduce the domain boundary energy. Second, the armchair structure of SnS should always be observed from its zigzag direction determined by "macroscopic" crystal shapes, as shown in Figure 4a. In our HAADF-STEM experiments, condition two is always fulfilled (in Figure 1b as well). Although four ferroelectric domain boundary candidates can be constructed based on the first condition, only one of them (type I-a) meets the second condition, as shown in Figure S10 (Supporting Information). Nevertheless, this type I-a structure is energetically unfavorable because two adjacent SnS crystals with opposite spontaneous polarizations are unlikely to bond directly with each other through S-S bonds. To reduce the overall energy, another plausible ferroelectric domain boundary structure with a NaCl structure in the boundary region is proposed, as shown in Figure 4c. The NaCl structure proposed here can serve as a transition phase to reduce boundary energy by avoiding bonding between the same species of atoms. It should be emphasized that the strip-shaped

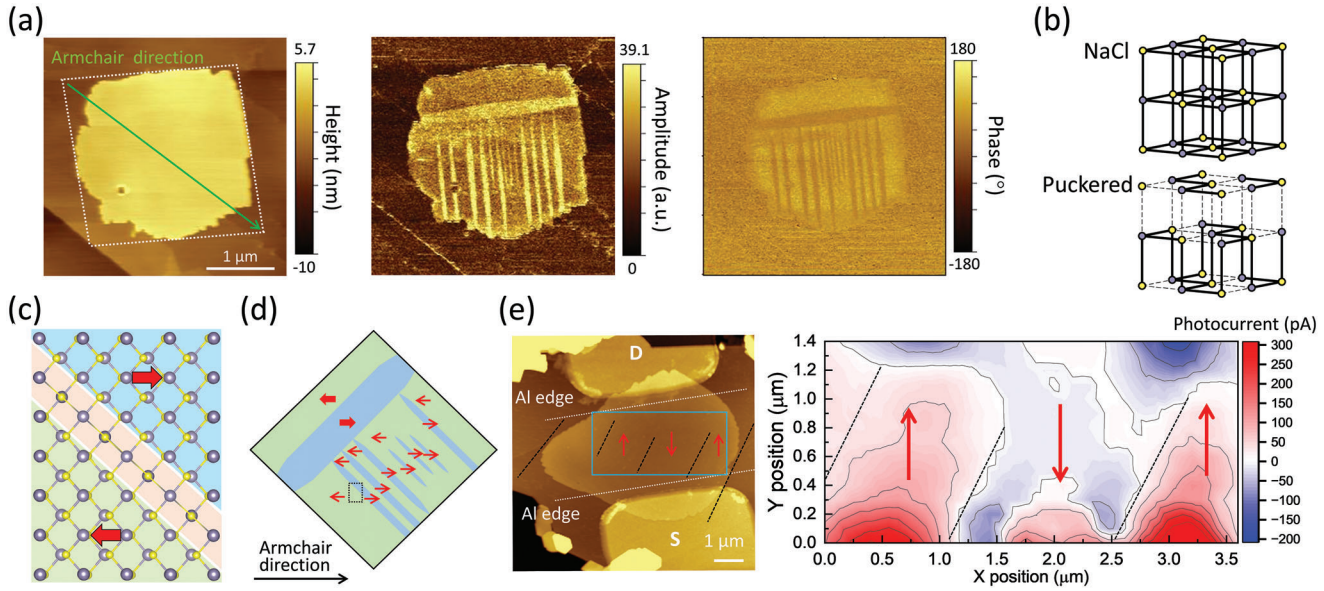

Figure 4. a) PFM height, amplitude, and phase images of few-layer SnS on HOPG substrate. The crystal orientation can be determined by the macroscopic shape of the crystal, as shown in the topographic image. b) Schematic illustrations of the NaCl and puckered structures. c) Proposed molecular model of the ferroelectric domain boundary of the dotted rectangular region shown in (d). The NaCl transition phase is proposed at the boundary of ferroelectric domains. The spontaneous polarization direction in SnS is denoted by red arrows. d) Schematic illustration of ferroelectric domains in SnS and their spontaneous polarization direction. e) AFM topographic image of a single-crystal SnS device and the photocurrent mapping in the marked channel region. The ferroelectric domain boundaries marked by black dotted lines are determined roughly by the region showing zero photocurrents. The ferroelectric domain boundaries are parallel to the energetically favorable facets of SnS.

orthogonal domains can be explained only using this proposed 180° domain structure without considering the 90° domain structure, as schematically illustrated in Figure 4d. Detailed discussions on the ferroelectric domain boundary structure are included in Figure S10 (Supporting Information).

Finally, to inspect the influence of ferroelectric domains on the photocurrent measurement, photocurrent mapping was conducted at the channel region of a single SnS crystal, as shown in Figure 4e. The negative (blue) and positive (red) photocurrent regions can be clearly distinguished in the same crystal. In accordance with the PFM results, this is caused by the existence of several ferroelectric domains with opposite spontaneous polarization, which also clarifies the reason for the small overall shift current compared to the theoretically predicted value of ≈100 μA V^{-2} for SnS.[29] While the ferroelectric domain boundary can be roughly defined by the areas with nearly zero photocurrents, these ferroelectric boundaries are parallel to the crystal facet plane as well. It should be noted that because of the limitation in laser spot size, the domain width (≈1 μm) obtained by optical mapping is much larger than that obtained from the PFM image shown in Figure 4a. Although more detailed characterization and analysis are needed, the accomplishment of this experiment provides the first discussion of the ferroelectric domain structure of SnS and the demonstration of ferroelectric domains through both piezoelectric response and optical approaches.

3. Conclusions

A non-centrosymmetric structure, which is likely to be induced and stabilized by surface stress, was observed in the bottom regions of PVD SnS crystals. This non-centrosymmetric structure is then confirmed to be the β' phase SnS by HAADF-STEM, Raman spectra, and SHG analyses. Assisted by Al film over the electrode contacts, the shift current along the armchair direction of SnS was obtained successfully. Through the polarization angle-dependent measurement and incident laser power-dependent measurement, the Schottky junction photocurrent and shift current of SnS could be distinguished clearly. Furthermore, the flow direction of shift current was determined with the support of CPGE current measurement even under the situation that the shift current was embedded by Schottky junction photocurrent. In the end, the ferroelectric domains of SnS were inspected by PFM as well as optical method and the atomic model of ferroelectric domain boundary in SnS was proposed. The β' phase SnS studied in this work can play an indispensable role in the future exploration of non-centrosymmetric properties in few-layer 2D materials.

4. Experimental Section

PVD Growth of SnS: A three-zone furnace with separate temperature controllers was used for the PVD growth of SnS, as schematically illustrated in Figure S1 (Supporting Information). SnS source powder (99.9%, Kojundo Chemical Laboratory Co.) was placed in Zone 1, while target substrates were placed in Zone 3. During the growth process, a 2.5 sccm pure N_2 gas (99.9995%) flow was used as the carrier gas, and the temperature difference between zone 1 and zone 3 was set to 20–80 °C to facilitate the transportation of the SnS source vapor. The pressure of the whole system was kept at 10 Pa during the growth processes. New surfaces of both mica and HOPG substrates were obtained by cleaving with Scotch tape before every growth round. For SnS growth on the *h*-BN substrate, multilayer *h*-BN flakes were mechanically exfoliated from bulk

crystals grown by a temperature-gradient method under a high-pressure and high-temperature atmosphere and transferred to a 90-nm SiO_2/n^+-Si substrate by the Scotch tape method.[67] Then, the substrates were annealed at 300 °C for 3 h to remove tape residue. Typical temperature profiles for SnS growth on the *h*-BN substrate and HOPG substrate were plotted as shown in Figure S1 (Supporting Information). The substrate temperatures for typical SnS growth on *h*-BN and HOPG substrates were 390 °C and 420–450 °C, respectively, while the growth time was 2–30 min. At the end of the growth process, the furnace temperature was quenched to <100 °C within 1 min to prevent further growth.

Characterization of SnS: AFM and PFM measurements were conducted on an Asylum Research Cypher HV at RT in a laboratory environment. For AFM, a 42 N m^{-1} Si cantilever was used, while a 2.8 N m^{-1} conductive tip coated with Pt/Ir was used for PFM. For the Raman spectroscopy measurements, the SnS samples were sealed in a cryostat chamber and cooled to 3 K in a vacuum of 0.01 Torr to prevent the thermal degradation and oxidation of SnS. A semiconductor laser with a wavelength of 488 nm was applied as the incident light with a focused spot size of 2.5 µm and an incident laser power of 1 mW after passing through an objective lens. The SHG analysis was conducted with a custom-built optical system under ambient conditions. A mode-locking femtosecond laser with a wavelength of 900 nm was applied as the incident light source with a focused spot size of 1 µm and an incident laser power of 0.3–0.9 mW before passing through an objective lens. Quantum Espresso[68] based on density functional theory was used to perform the first-principle calculation of electronic band structure of bilayer β' SnS. A $14 \times 14 \times 1$ *k*-mesh was used for sampling the Brillouin zone. The results of SHG were calculated by solving the time-dependent Bethe Salpeter equation in Yambo code.[69] For the cross-sectional HAADF-STEM analysis of SnS, the focused ion beam (FIB) technique was used to prepare sample cross-sections. The cross-sectional images of SnS were obtained using a JEM-ARM200F (JEOL) electron microscope at an accelerating voltage of 200 kV.

Device Fabrication: For shift-current device fabrication, a maskless aligner with double layer resists (PMGI SF5/AZ1500) and an NMD-3 developer were used to define electrode patterns. A 1 nm/20 nm Ti/Au electrode was deposited in an ultrahigh vacuum (UHV) chamber at a base pressure of $\approx 5 \times 10^{-8}$ Pa with a low deposition rate of 0.0014 Å s^{-1} for Ti and 0.15 Å s^{-1} for Au. Then, 10–20 nm-thick *h*-BN flakes were transferred on top of the channel region of the SnS device as an encapsulation layer by a dry transfer method using poly(dimethylsiloxane) (PDMS) films.[70] Finally, ≈50 nm-thick Al was deposited on top of the contact region between the metal electrode and SnS by thermal evaporation at a vacuum level of 10^{-5} Pa.

Photocurrent Measurement: SnS devices were placed under a commercial optical microscopy (OM) system, as shown in Figure S7 (Supporting Information). A semiconductor laser with a wavelength of 488 nm and an ideal spot size of 0.66 µm was used to stimulate the photocurrent, while the electrical properties were measured by a Keysight B1500 semiconductor analyzer. To prevent the sample position from shifting physically during the relatively long-time line-scan/mapping experiments, the electrodes of SnS devices were extended by gold wires, and the probes were in contact with the device electrode outside of the sample stage of the OM system. The polarization angle dependence measurement of the shift current was performed by applying a half-wave plate to a linearly polarized laser. The line-scan/mapping measurements of the photocurrent were performed with a DMD, where the optical light was scanned while keeping the sample stationary. During the CPGE current measurement, a quarter-wave plate was applied to generate circularly polarized light. The laser power-dependent experiment was conducted using a variable neutral density (ND) filter.

Supporting Information

Supporting Information is available from the Wiley Online Library or from the author.

Acknowledgements

The authors thank Shunto Arai for helpful discussion on PFM measurement. This research was supported by the Mitsubishi Foundation, NEXCO Group Companies' Support Fund to Disaster Prevention Measures on Expressways, the JSPS A3 Foresight Program, JSPS KAKENHI (Grant Numbers: JP22H04957, JP21H05237, JP21H05235, JP21H05233, JP21H05232, JP22K18986, JP20H05664, and JP21H01012), NICT (Grant Number: 05901), JST-Mirai Program (Grant Number: JPMJMI22708192), and the JST FOREST program (Grant Number: JPMJFR213K), Japan.

Conflict of Interest

The authors declare no conflict of interest.

Data Availability Statement

The data that support the findings of this study are available from the corresponding author upon reasonable request.

Keywords

2D materials, ferroelectric domains, non-centrosymmetry, shift currents, tin sulfide

Received: February 6, 2023
Revised: April 16, 2023
Published online: June 2, 2023

[1] P. S. Brody, *J. Solid State Chem.* **1975**, *12*, 193.
[2] B. Sturman, V. Fridkin, *The Photovoltaic and Photorefractive Effects in Noncentrosymmetric Materials*, Routledge, London, UK, **1992**.
[3] J. T. Zhang, W. N. Zhao, P. Yu, G. W. Yang, Z. Liu, *2D Mater.* **2020**, *7*, 042002.
[4] H. Khan, N. Mahmood, A. Zavabeti, A. Elbourne, M. A. Rahman, B. Y. Zhang, V. Krishnamurthi, P. Atkin, M. B. Ghasemian, J. Yang, G. Zheng, A. R. Ravindran, S. Walia, L. Wang, S. P. Russo, T. Daeneke, Y. Li, K. Kalantar-Zadeh, *Nat. Commun.* **2020**, *11*, 3449.
[5] W. Z. Wu, L. Wang, Y. L. Li, F. Zhang, L. Lin, S. M. Niu, D. Chenet, X. Zhang, Y. F. Hao, T. F. Heinz, J. Hone, Z. L. Wang, *Nature* **2014**, *514*, 470.
[6] N. Higashitarumizu, H. Kawamoto, C.-J. Lee, B.-H. Lin, F.-H. Chu, I. Yonemori, T. Nishimura, K. Wakabayashi, W.-H. Chang, K. Nagashio, *Nat. Commun.* **2020**, *11*, 2428.
[7] K. Yasuda, X. R. Wang, K. Watanabe, T. Taniguchi, P. Jarillo-Herrero, *Science* **2021**, *372*, 1458.
[8] L. You, Y. Zhang, S. Zhou, A. Chaturvedi, S. A. Morris, F. C. Liu, L. Chang, D. Ichinose, H. Funakubo, W. J. Hu, T. Wu, Z. Liu, S. Dong, J. L. Wang, *Sci. Adv.* **2019**, *5*, eaav3780.
[9] Y. J. Zhang, T. Ideue, M. Onga, F. Qin, R. Suzuki, A. Zak, R. Tenne, J. H. Smet, Y. Iwasa, *Nature* **2019**, *570*, 349.
[10] T. Akamatsu, T. Ideue, L. Zhou, Y. Dong, S. Kitamura, M. Yoshii, D. Y. Yang, M. Onga, Y. Nakagawa, K. Watanabe, T. Taniguchi, J. Laurienzo, J. W. Huang, Z. L. Ye, T. Morimoto, H. T. Yuan, Y. Iwasa, *Science* **2021**, *372*, 68.
[11] Y. Li, J. Fu, X. Y. Mao, C. Chen, H. Liu, M. Gong, H. L. Zeng, *Nat. Commun.* **2021**, *12*, 5896.
[12] C. J. Cui, F. Xue, W. J. Hu, L. J. Li, *npj 2D Mater. Appl.* **2018**, *2*, 18.
[13] W. B. Choi, J. Y. Kim, E. H. Lee, G. Mehta, V. Prasad, *ACS Appl. Mater. Interfaces* **2021**, *13*, 13596.

[14] Z. Li, Y. Zhao, W. L. Li, Y. Z. Peng, W. Y. Zhao, Z. Wang, L. Shi, W. D. Fei, *J. Mater. Chem. A* **2022**, *10*, 8772.
[15] Y. Zhang, P. Huang, J. Guo, R. C. Shi, W. C. Huang, Z. Shi, L. M. Wu, F. Zhang, L. F. Gao, C. Li, X. W. Zhang, J. L. Xu, H. Zhang, *Adv. Mater.* **2020**, *32*, 2001082.
[16] L. F. Gao, C. Y. Ma, S. R. Wei, A. V. Kuklin, H. Zhang, H. Agren, *ACS Nano* **2021**, *15*, 954.
[17] J. Wang, J. Y. Han, X. Q. Chen, X. R. Wang, *Infomat* **2019**, *1*, 33.
[18] X. He, Y. Iwamoto, T. Kaneko, T. Kato, *Sci. Rep.* **2022**, *12*, 11315.
[19] S. Y. Yang, J. Seidel, S. J. Byrnes, P. Shafer, C. H. Yang, M. D. Rossell, P. Yu, Y. H. Chu, J. F. Scott, J. W. Ager, L. W. Martin, R. Ramesh, *Nat. Nanotechnol.* **2010**, *5*, 143.
[20] W. Shockley, H. J. Queisser, *J. Appl. Phys.* **1961**, *32*, 510.
[21] B. M. Fregoso, *Phys. Rev. B* **2019**, *100*, 064301.
[22] T. Morimoto, N. Nagaosa, *Sci. Adv.* **2016**, *2*, 1501524.
[23] D. Niesner, M. Hauck, S. Shrestha, I. Levchuk, G. J. Matt, A. Osvet, M. Batentschuk, C. Brabec, H. B. Weber, T. Fauster, *Proc. Natl. Acad. Sci. USA* **2018**, *115*, 9509.
[24] X. J. Liu, A. Chanana, U. Huynh, F. Xue, P. Haney, S. Blair, X. M. Jiang, Z. V. Vardeny, *Nat. Commun.* **2020**, *11*, 323.
[25] S. Barraza-Lopez, B. M. Fregoso, J. W. Villanova, S. S. P. Parkin, K. Chang, *Rev. Mod. Phys.* **2021**, *93*, 011001.
[26] J. Jiang, Z. Z. Chen, Y. Hu, Y. Xiang, L. F. Zhang, Y. P. Wang, G. C. Wang, J. Shi, *Nat. Nanotechnol.* **2021**, *16*, 894.
[27] A. M. Burger, L. Y. Gao, R. Agarwal, A. Aprelev, J. E. Spanier, A. M. Rappe, V. M. Fridkin, *Phys. Rev. B* **2020**, *102*, 081113.
[28] R. Resta, *Rev. Mod. Phys.* **1994**, *66*, 899.
[29] T. Rangel, B. M. Fregoso, B. S. Mendoza, T. Morimoto, J. E. Moore, J. B. Neaton, *Phys. Rev. Lett.* **2017**, *119*, 067402.
[30] H. Wang, X. F. Qian, *Sci. Adv.* **2019**, *5*, eaav9743.
[31] N. T. Kaner, Y. D. Wei, Y. J. Jiang, W. Q. Li, X. D. Xu, K. J. Pang, X. J. Li, J. Q. Yang, Y. Y. Jiang, G. L. Zhang, W. Q. Tian, *ACS Omega* **2020**, *5*, 17207.
[32] M. H. Wu, X. C. Zeng, *Nano Lett.* **2016**, *16*, 3236.
[33] H. Wang, X. F. Qian, *2D Mater.* **2017**, *4*, 015042.
[34] N. Higashitarumizu, H. Kawamoto, K. Ueno, K. Nagashio, *MRS Adv.* **2018**, *3*, 2809.
[35] R. X. Fei, W. Kang, L. Yang, *Phys. Rev. Lett.* **2016**, *117*, 097601.
[36] Y. Bao, P. Song, Y. P. Liu, Z. H. Chen, M. L. Zhu, I. Abdelwahab, J. Su, W. Fu, X. Chi, W. Yu, W. Liu, X. X. Zhao, Q. H. Xu, M. Yang, K. P. Loh, *Nano Lett.* **2019**, *19*, 5109.
[37] Y. R. Chang, N. Higashitarumizu, H. Kawamoto, F. H. Chu, C. J. Lee, T. Nishimura, R. Xiang, W. H. Chang, S. Maruyama, K. Nagashio, *Chem. Mater.* **2021**, *33*, 186.
[38] P. Sutter, R. Ibragimova, H. P. Komsa, B. A. Parkinson, E. Sutter, *Nat. Commun.* **2019**, *10*, 5528.
[39] B. Xu, J. K. Deng, X. D. Ding, J. Sun, J. Z. Liu, *npj Comput. Mater.* **2022**, *8*, 47.
[40] A. N. Mehta, H. Zhang, A. Dabral, O. Richard, P. Favia, H. Bender, A. Delabie, M. Caymax, M. Houssa, G. Pourtois, W. Vandervorst, *J Microsc* **2017**, *268*, 276.
[41] M. Devika, N. K. Reddy, F. Patolsky, K. Ramesh, K. R. Gunasekhar, *Appl. Phys. Lett.* **2009**, *95*, 261907.
[42] *Engineering ToolBox, Thermal Expansion – Linear Expansion Coefficients*, **2003**.
[43] C. Androulidakis, C. Galiotis, *2D Mater.* **2020**, *7*, 045011.
[44] G. H. Ahn, M. Amani, H. Rasool, D. H. Lien, J. P. Mastandrea, J. W. Ager, M. Dubey, D. C. Chrzan, A. M. Minor, A. Javey, *Nat. Commun.* **2017**, *8*, 608.
[45] I. Yonemori, S. Dutta, K. Nagashio, K. Wakabayashi, *AIP Adv.* **2021**, *11*, 095106.
[46] N. Higashitarumizu, H. Kawamoto, M. Nakamura, K. Shimamura, N. Ohashi, K. Ueno, K. Nagashio, *Nanoscale* **2018**, *10*, 22474.
[47] Y.-R. Chang, T. Nishimura, T. Taniguchi, K. Watanabe, K. Nagashio, *ACS Appl. Mater. Interfaces* **2022**, *14*, 19928.
[48] W. Nishiyama, T. Nishimura, K. Ueno, T. Taniguchi, K. Watanabe, K. Nagashio, *Adv. Funct. Mater.* **2022**, *32*, 2108061.
[49] H. Kawamoto, N. Higashitarumizu, N. Nagamura, M. Nakamura, K. Shimamura, N. Ohashi, K. Nagashio, *Nanoscale* **2020**, *12*, 23274.
[50] M. Fabian, E. Lewis, T. Newe, S. Lochmann, *Meas. Sci. Technol.* **2010**, *21*, 094034.
[51] Y. Cui, Z. Q. Zhou, X. H. Wang, X. T. Wang, Z. H. Ren, L. F. Pan, J. H. Yang, *Nano Res.* **2021**, *14*, 2224.
[52] V. I. Belinicher, B. I. Sturman, *Usp. Fiz. Nauk* **1980**, *130*, 415.
[53] Y. Peng, X. T. Liu, Z. H. Sun, C. M. Ji, L. N. Li, Z. Y. Wu, S. S. Wang, Y. P. Yao, M. C. Hong, J. H. Luo, *Angew. Chem., Int. Ed.* **2020**, *59*, 3933.
[54] A. Bhatnagar, A. R. Chaudhuri, Y. H. Kim, D. Hesse, M. Alexe, *Nat. Commun.* **2013**, *4*, 2835.
[55] J. Y. Wang, H. P. Lu, X. Pan, J. W. Xu, H. L. Liu, X. J. Liu, D. R. Khanal, M. F. Toney, M. C. Beard, Z. V. Vardeny, *ACS Nano* **2021**, *15*, 588.
[56] T. Zhu, J. Bie, C. Ji, X. Zhang, L. Li, X. Liu, X.-Y. Huang, W. Fa, S. Chen, J. Luo, *Nat. Commun.* **2022**, *13*, 7702.
[57] J. H. Su, X. T. Wang, C. Shao, Y. Z. Guo, L. D. Xian, *Mater. Des.* **2021**, *209*, 110005.
[58] Y. Zhang, R. Taniguchi, S. Masubuchi, R. Moriya, K. Watanabe, T. Taniguchi, T. Sasagawa, T. Machida, *Appl. Phys. Lett.* **2022**, *120*, 013103.
[59] S. M. Young, A. M. Rappe, *Phys. Rev. Lett.* **2012**, *109*, 116601.
[60] G. Arlt, *Ferroelectrics* **1990**, *104*, 217.
[61] S. Katayama, Y. Noguchi, M. Miyayania, *Adv. Mater.* **2007**, *19*, 2552.
[62] P. Sutter, H. P. Komsa, H. Lu, A. Gruverman, E. Sutter, *Nano Today* **2021**, *37*, 101082.
[63] K. Chang, F. Kuster, B. J. Miller, J. R. Ji, J. L. Zhang, P. Sessi, S. Barraza-Lopez, S. S. P. Parkin, *Nano Lett.* **2020**, *20*, 6590.
[64] M. E. Lines, A. M. Glass, Principles and Applications of Ferroelectrics and Related Materials, Oxford University Press, Oxford, UK **2001**.
[65] R. Hoffmann, *Angew. Chem., Int. Ed.* **1987**, *26*, 846.
[66] D. B. Holt, *J. Mater. Sci.* **1984**, *19*, 439.
[67] K. Watanabe, T. Taniguchi, H. Kanda, *Nat. Mater.* **2004**, *3*, 404.
[68] P. Giannozzi, S. Baroni, N. Bonini, M. Calandra, R. Car, C. Cavazzoni, D. Ceresoli, G. L. Chiarotti, M. Cococcioni, I. Dabo, A. Dal Corso, S. de Gironcoli, S. Fabris, G. Fratesi, R. Gebauer, U. Gerstmann, C. Gougoussis, A. Kokalj, M. Lazzeri, L. Martin-Samos, N. Marzari, F. Mauri, R. Mazzarello, S. Paolini, A. Pasquarello, L. Paulatto, C. Sbraccia, S. Scandolo, G. Sclauzero, A. P. Seitsonen, et al., *J. Phys.: Condens. Matt.* **2009**, *21*, 395502.
[69] A. Marini, C. Hogan, M. Gruning, D. Varsano, *Comput. Phys. Commun.* **2009**, *180*, 1392.
[70] S. Toyoda, T. Uwanno, T. Taniguchi, K. Watanabe, K. Nagashio, *Appl. Phys. Express* **2019**, *12*, 055008.